TRENDS IN SCIENCES 2026; 23(3): 11913
https://doi.org/10.48048/tis.2026.11913 RESEARCH ARTICLE

Oxygen-Enriched Air from Natural-Zeolite PSA to Improve Al–Air Battery Discharge Performance

Haji Aripin[1,*], Rahmat Rizal[1], Irwan Muhammad Ridwan[1], I Nyoman Sudiana[2] and Svilen Sabchevski[3]

[1]Department of Physics Education, Faculty of Teacher Training and Education, Siliwangi University, West Java 46115, Indonesia
[2]Department of Physics, Faculty of Mathematics and Natural Sciences, Haluoleo University, Kendari 93232, Indonesia
[3]Lab. Plasma Physics and Engineering, Institute of Electronics of the Bulgarian Academy of Sciences, Sofia 1784, Bulgaria

([*]Corresponding author's e-mail: aripin@unsil.ac.id)

Received: 16 September 2025, Revised: 5 October 2025, Accepted: 12 October 2025, Published: 20 December 2025

Abstract

In the present study, oxygen-rich air produced from ambient air over a zeolite adsorbent by a pressure swing adsorption (PSA) system has been investigated for use as a cathode source in aluminum-air (Al-air) batteries. Four types of natural zeolite adsorbent samples were prepared by varying the microwave heating time at a frequency of 2.45 GHz between 30 and 120 min. The synthesized samples were characterized using scanning electron microscopy (SEM) and N_2 adsorption-desorption isotherms. The samples were tested to measure the degree of oxygen purity produced by the PSA system. The performance of the produced oxygen was tested as a cathode in discharge experiments in an Al-air battery. The effect of oxygen purity on the cell's discharge performance was investigated by analyzing the increased amount of discharge products formed on the porous TiO_2 cathode. It has been found that the samples prepared with a heating time of 60 min had the highest volume of mesoporous structures and thus generated an oxygen purity of 73.01%. Additionally, the amount of discharge products formed on the porous TiO_2 cathode decreases as oxygen purity increases. At an oxygen purity of 73.01%, the lowest percentage of discharge products was found bound to the porous TiO_2 cathode surface. This results in a cathode with the highest proportion of mesoporous volume and the highest discharge capacity value of 817.12 mAh/g.

Keywords: Oxygen-rich air, Zeolite adsorbent, PSA, Heating time, Discharge products, Al-air batttery, Discharge capacity

Introduction

Oxygen is a crucial gaseous element with multiple applications across various industrial processes. These include biofuel production [1,2], medical oxygen as a life-saving treatment [3], oxy-coal combustion with CO_2 capture [4], as well as electrochemical energy conversion and storage technologies such as batteries [5]. The latter, particularly metal-air batteries, has been actively studied as a promising energy conversion and storage solution for energy transfer stations in renewable energy production. These batteries deliver an operating voltage as high as 3.4 V [6], generate an ultra-high capacity of approximately 821 mAh/g at 0.1 C [7] and achieve more than 86% efficiency over 100 cycles [8]. Such favorable parameters are accompanied by several technological advantages, reduced as a reduced battery weight, the ability to store large amounts of electric energy in a small volume and a lower risk of inflammation, as well as economic advantages such as the use of abundant oxygen from ambient air and reduced use of disposable and harmful metal-containing components. These characteristics support the

possibility of replacing the currently used lithium (Li-ion), Ni-MH, and lead-acid batteries as storage and conversion media for the portable electronic and wearable devices widely used nowadays.

One of the most mature and promising metal-air batteries is the aluminium-air battery (Al-air battery). The Al-air battery is notable for its theoretical parameters such as high-capacity density of about 2.98 Ah/g, an operating voltage of 2.7 V and maximum energy density of 8.1 kWh/kg [9]. The abundance and low cost of Al as an anode material givesthis type of battery a significant advantage over other metal-air batteries. Therefore, Al-air batteries are considered feasible, viable and economically beneficial.

Extensive research has been focused on the electrochemical properties of the Al-air batteries. A variation of guar gum (GG) binder content in graphite/SX has been prepared for use as an active cathode in Al-air batteries [10]. This study has demonstrated that a battery cell plate voltage of around 1.1 V and a maximum cell capacity of the battery of 42 mAh/g have been achieved. Furthermore, varying the SX and graphite content in the cathode layer [11] resulted in a cell voltage of about 1.05 V and a maximum capacity of about 45 mAh/g. In another study, kaolin mixed with KOH was prepared as a quasi-solid-state electrolyte in an Al-air battery [9]. The uniform pore channels of kaolin successfully increased the mass transfer of OH- and oxygen within the air cathode. This Al-air battery achieved an operating voltage of about 1.24 V and a specific capacity of 175.1 mAh/g. These results demonstrated experimentally that the nominal stable voltage and discharge capacity of a single Al-air cell range from 0.8 to 1.3 V and 20 to 175.1 mAh/g, respectively. When the air cathode with many well-distributed pores is exposed to oxygen, positive changes (an increase in the discharge voltage and capacity) are observed in an Al-air battery.

Currently, the O_2 supply for Al-air batteries is sourced from ambient air. In addition to O_2, ambient air contains non-O_2 gases such as N_2, Ar, H_2O and CO_2. These components affect the reaction mechanism of Al-air batteries. The presence of N_2 and Ar in the battery inhibits the activation of electrochemical reactions when operated at a battery cathode voltage of around 3 V [12]. CO_2 can undergo electrochemical reactions with Al to form $Al_2(CO_3)_3$, which limits the cycling capability of the Al-air batteries [13]. Therefore, these components must be removed from the gas stream before it enters the battery. Thus, a high-purity O_2 gas production technology is needed to supply Al-air batteries.

Several technologies, such as cryogenic distillation, membrane separation, and pressure swing adsorption (PSA), are used to separate O_2 gas from ambient air. Cryogenic distillation produces high-purity O_2 gas of over 99% [14], but the unstable purity of O_2 gas limits its suitability for meeting the O_2 supply requirements of Al-O_2 batteries. Membrane separation produces a high purity level of 96% [15] but requires higher pressure and expensive selective permeable materials. The PSA system provides O_2 gas generation at a stable purity of around 93% [16], making it an on-demand source for Al-O_2 battery applications.

Many studies have investigated air separation by PSA using different adsorbents for O_2 production. The performance of adsorbent materials in PSA has been evaluated using 5A zeolite and 13X zeolite [17], LiX zeolite [18] and LiLSX zeolite [19]. The 2-bed and 2-step PSA systems have used zeolites with surface areas of 20 - 50 m^2/g and operating pressures of 1.5 - 4 bar. These studies have shown that the PSA system can produce O_2 with concentrations up to 90%. This is because zeolites tend to absorb twice as much N_2 as O_2 due to the cation bonding of zeolite molecules and the quadrupole moment of N_2. The zeolites used in some studies, as mentioned above, are synthetic and available in commercial quantities. Due to the high cost of synthetic zeolite for PSA applications, we envisage that it could be replaced by the natural zeolites [20-22]. The main advantages of these natural zeolites are as follows. First, as a natural mineral resource, they are low-cost and abundantly available, reducing the cost of the adsorbent. Second, the use of zeolite provides both microporous and mesoporous structures with tube-like channels and high Al content [23]. Both factors suggest that they have potential as PSA adsorbent materials. This work aims to experimentally determine the appropriate technological parameters to produce high-purity oxygen from ambient air using Karangnunggal zeolite as an adsorbent in the PSA system. Additionally, we also discuss the use of generated oxygen as an oxygen cathode of Al-air batteries and the effect of their purity on the discharge capacity.

Materials and methods

Preparing the zeolite

Natural zeolite was collected from Karangnunggal District, Tasikmalaya Regency, West Java Province, Indonesia. The zeolite was manually cleaned by washing with water, then dried in sunlight. Furthermore, the zeolite was crushed into small pieces and ground using a ball mill to obtain a uniform and fine particle size from 0.5 to 1.0 mm. Fifty grams of the zeolite sample were mixed with a dilute 5 M NaOH solution and stirred for 60 min. The mixture was filtered using Whatman filter paper No. 41 and washed with distilled water 8 - 10 times to remove residual Na_2 cations. Four types of samples were prepared by 2.45 GHz microwave heating at a temperature of 110 °C and heating times of 30, 60, 90 and 120 min. Based on the heating time, the samples were designated as Z-30, Z-60, Z-90 and Z-120, respectively. The prepared dry samples were stored in a desiccator to prevent contamination and prepare for further analysis.

Measuring oxygen purity level

The PSA system comprises a reciprocating compressor, a heat exchanger tube, a dryer tube, an adsorption column, an oxygen storage tube, and an oxygen sensor. The column bed is made of stainless steel, with a length of 0.5 m and an inner diameter of 70 mm. Each column is filled with approximately 1,000 g of a Z-30 adsorbent sample.

Atmospheric air enters the compressor and is compressed to a pressure of 10 bar. The compressed air is then cooled down by passing through a heat exchanger. Before entering the PSA columns, water is removed from the air using active silica xerogel in a dryer tube. Next, the dry air stream is fed through the first column at high pressure, where adsorption occurs. During this process, the zeolite selectively absorbs nitrogen gas from the air. The outlet stream from the first column is obtained as oxygen-enriched gas (OEG). The OEG is split into two streams: First passes to an oxygen sensor (GOX 100 Greisinger Electronic GmbH), which detects the presence of oxygen concentration as a percentage of the flow volume and the second is directed to an oxygen storage tube. Simultaneously, the pressure in the second column is reduced to remove the nitrogen gas trapped in the zeolite. Operation alternates between the 2 columns. Testing of Z-60, Z-90, and Z-120 samples was conducted following the same procedure.

Testing the performance of a prepared oxygen cathode in an Al-air battery

In this experiment, the prepared Al-air battery cell is identical to that described in a previous study [24]. The cathode material of the cell consists of a mixture of an active layer of TiO_2, carbon black (CB) and a polyvinylidene fluoride (PVDF) binder in a weight ratio of 8:1:1. CB and PVDF powders are commercially available materials supplied by Sigma Aldrich. N-methyl-2-pyrrolidone (NMP, Sigma-Aldrich, 99.5%) was used to dissolve PVDF and disperse TiO_2 and CB to form uniform slurry. Residual NMP in the slurry was removed by drying in an oven at 110 °C for 12 h.

The anode and cathode are arranged in parallel in an Al-air battery cell with an active area of approximately 16 cm^2, separated by a polypropylene (PP) separator. The anode material is an aluminium (Al) plate of alloy 1,100 and the cathode material is the slurry attached to a Ni mesh substrate. The electrolyte is a concentrated KOH solution of 6 M.

The assembled cells were placed in a rectangular chamber module filled with oxygen supplied from the PSA system. Experimental tests have been performed to estimate the discharge pattern of a single Al-air battery cell. In this experiment, the purity of oxygen gas for the cathode varied from 21% to 73.01%. Oxygen gas from the storage cylinder in the PSA system is flowed into the sealed rectangular chamber module with a flow rate of 0.1 L/min. Discharge tests at 10 mA of Al-air cell were carried out using a multichannel battery testing system (BTS-MPTS, China).

Methodology for characterizing samples

The X-ray diffraction of a Karangnunggal natural zeolite sample has been carried out using a Smartlab X-ray diffractometer with filtered Cu Kα radiation at a wavelength of 0.15418 nm and a measurable trace range from 10 to 90 degrees. The microstructures of the samples obtained after microwave heating were imaged using a JEOL JSM-6400 scanning electron microscope (SEM) at a magnification of 10,000 times. Adsorption-desorption isotherms of nitrogen and pore size distribution in the samples were measured at 77 K and analysed using a Quantachrome Nova-1000 pore size

analyzer. Functionalization reactions in the cathode material samples of TiO_2 after discharge treatment were examined by FTIR spectroscopy at room temperature using the KBr pellet technique. FTIR spectral reflectance data were recorded in the range of 4,000 to 400 cm^{-1} at a resolution of 4 cm^{-1}.

Results and discussion

Table 1 shows the percentage of various oxides for the Karangnunggal natural zeolite sample. SiO_2 is present in the largest proportion, at about 74.75%. In addition, significant amounts of MgO, Al_2O_2, Na_2O and CaO are found in the zeolite. The loss on ignition (LOI) of about 1.27% is attributed to additional volatile components, hydroxides and organic matter in the sample.

Table 1 Percentage of various oxides in the Karangnunggal zeolite.

Oxide elements	Zeolite (wt.%)
SiO_2	74.75
TiO_2	0.15
MnO	0.02
MgO	7.92
Al_2O_3	12.52
Na_2O	2.26
Fe_2O_3	0.91
K_2O	0.21
CaO	1.25
LOI	1.27

Figure 1 presents the XRD pattern of the untreated Karangnunggal natural zeolite sample. It can be seen that, in the zeolite sample, peaks observed at 2θ = 9.7°, 11.2°, 12.9°, 17.2°, 19.0°, 19.6°, 21.8°, 22.4°, 25.6°, 26.2°, 27.2°, 30.0° and 32.4° are assigned to the zeolitic phase type clinoptilolite. In the same sample, other peaks at 2θ = 20.8°, 26.8° and 35.6° are identified as the quartz phase. These results are consistent with those for natural zeolite derived from Klaten zeolite [25]. The XRD pattern analysis demonstrates the effectiveness of natural zeolite as adsorbent raw material in the PSA system for oxygen production proposed by us.

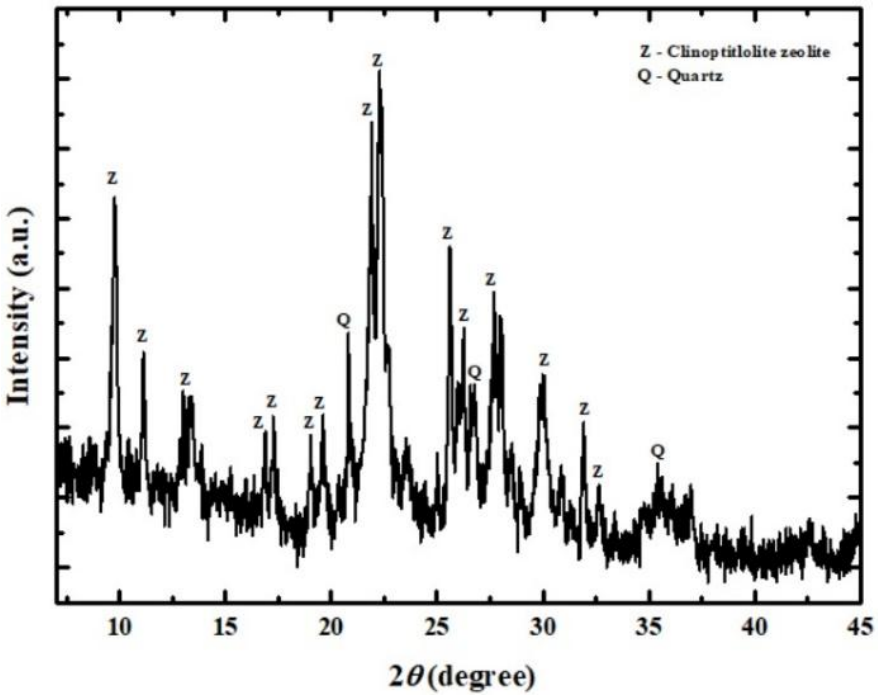

Figure 1 The XRD pattern of the Karangnunggal natural zeolite sample without treatment.

Figure 2 shows SEM images of the zeolite samples heated by microwaves for different durations. In the Z-30 sample (**Figure 2(a)**), the microstructure displays rough, bumpy surface textures and inhomogeneous pores. Many closed pores are present and large pores are loosely connected. This is likely due to the presence of water-filled pores and organic residues that have not fully volatilized or combusted in all pores. In this case, water may evaporate and organic residues may combust from the pores on the external surfaces, but not yet form the interior pores. This image is consistent with the SEM results observed for samples treated by water drying [26]. In the Z-60 sample, the increased heating time results in a much more homogeneous pore distribution. Consequently, the structure becomes highly porous with a network of open, interconnected and regular pores. These pores originate from the empty spaces left by both water evaporation and combustion of organic residues on the external surfaces and within the interior of the porous wall, leading to a natural increase in the number of empty pores.

The surface modifications in the Z-90 and Z-120 samples show smaller, heterogeneous pore shapes on the sample surfaces, making the surface appear denser. We suppose that its presence is due to the large growth of sintering neck between adjacent particles in the samples, which created particles in a powder compact bond together under heating [27]. The number of pores in the pore wall was significantly reduced and the samples formed a more compact microstructure.

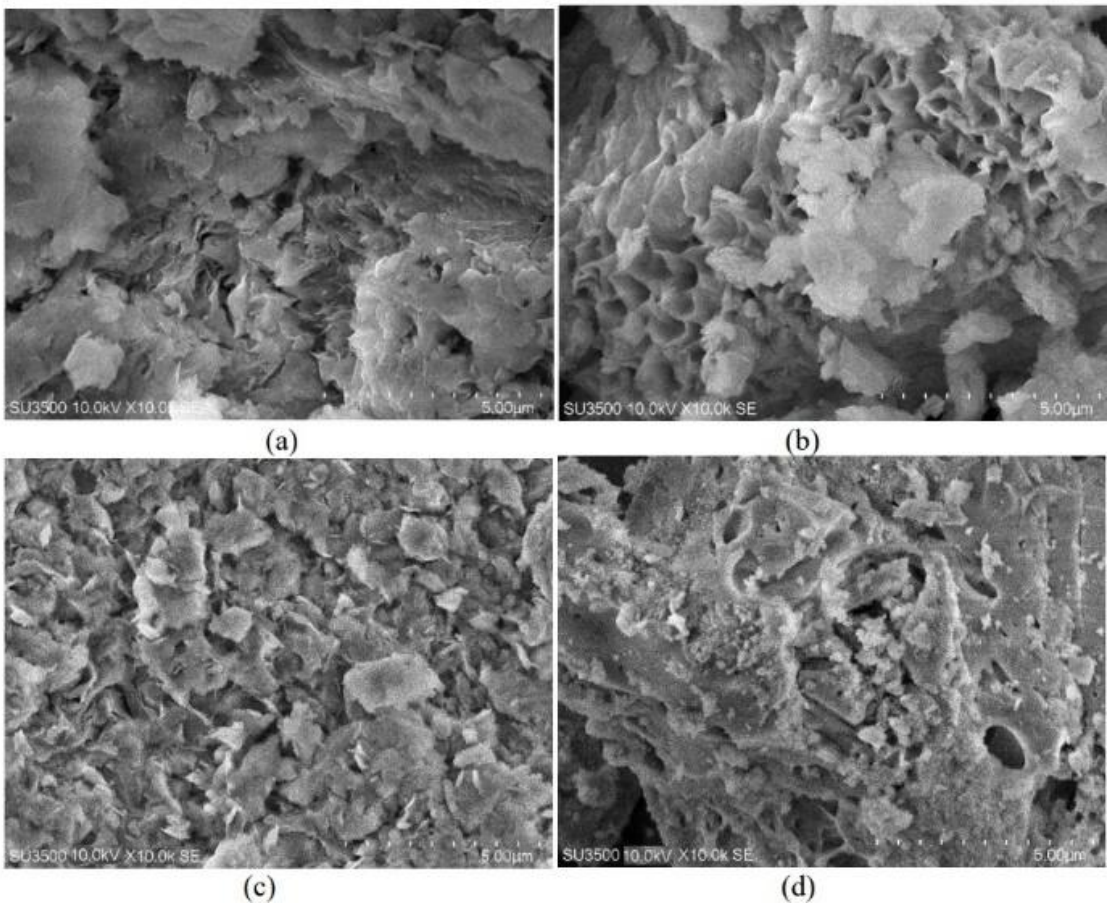

Figure 2 SEM images for zeolite samples of (a) Z-30, (b) Z-60, (c) Z-90 and (d) Z-120.

Figures 3(a) - 3(b) show the adsorption-desorption isotherms of nitrogen at 77 K and the pore size distribution for zeolite samples prepared by microwave treatment for different durations, respectively. According to the International Union of Pure and Applied Chemistry (IUPAC) classification, the adsorption-desorption isotherms of nitrogen for all samples exhibit a type IV isotherm with a similar H3-type hysteresis loop [28], which is characteristic of a slit-shaped mesoporous structure. In **Figure 3(a)**, adsorption initially occurs at low relative pressure (P/Po) of around 0.02 due to nitrogen filling the micropores. As P/Po increases to 0.4, adsorption rises slowly without reaching saturation. Further increasing P/Po from 0.4 to 0.9 leads to greater adsorption by the samples. This behaviour results from the presence of mesopores formed in interparticle voids and parallel plate-shaped pores. A sharp increase in adsorbed nitrogen at P/Po above 0.95 indicates the presence of more macropores. However, the desorption curve does not coincide with the adsorption curve, forming a narrow hysteresis loop until a P/Po point at about 0.4 on the adsorption curve. This loop arises from the difference in condensation and evaporation processes caused by the pore texture [29]. At the closure position of the desorption curve (P/Po = 0.4) possibly, this is because the absorbed nitrogen gas cannot be released from the pores with widths equal to that of nitrogen molecules. This phenomenon is in line with the research by [30], which found that low P/Po hysteresis occurs when micropore-sized samples are comparable to the size of nitrogen molecules. Furthermore, the hysteresis loop width increases for samples from Z-30 to Z-60 and decreases for samples from Z-60 to Z-120. The increase and decrease in loop width are attributed to a non-uniform pore size distribution and the reduced pore size of the sample as heating time increases, respectively. This mechanism is supported by the results of a study in mesoporous silica [31] which revealed that changes in pore size and its distribution in mesopore-sized samples led to changes in the hysteresis loop width.

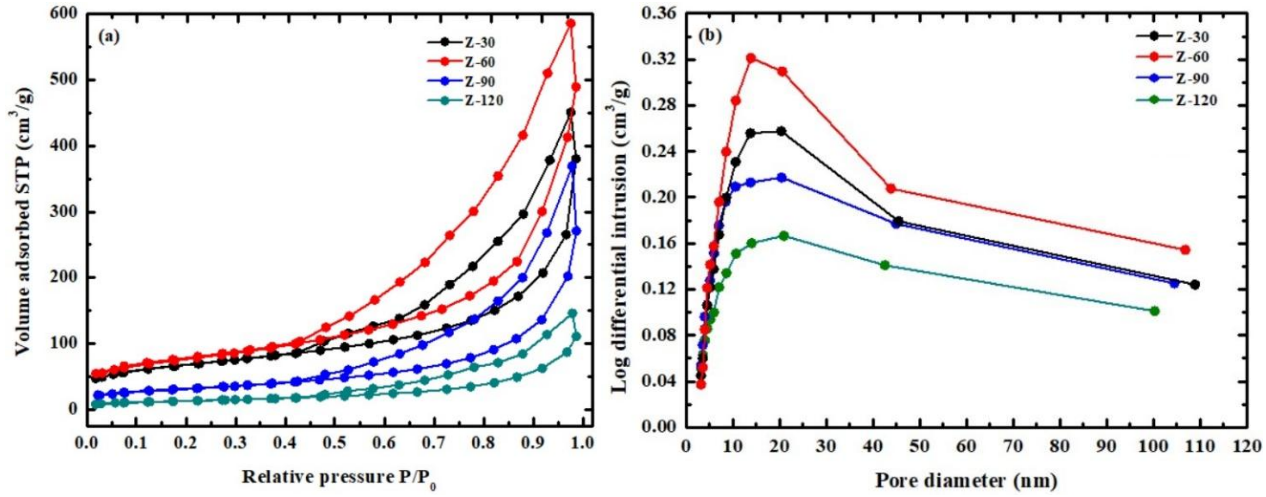

Figure 3 Curves of (a) adsorption-desorption isotherms of nitrogen and (b) a pore size distribution for zeolite samples prepared by microwave treatment at different times.

The nitrogen gas uptake increases for samples from Z-30 to Z-60 and decreases for samples from Z-60 to Z-120, which may be attributed to the production of a high ratio of mesopore volume to total pore volume. In **Figure 3(b)**, the PSD of all samples shows unimodal pore size distributions, with the larger mesopores centred at about 15 nm. All samples have similar pore size distributions, composed of a combination of micro-, meso- and macroporous structures. However, the microporous structure is still present in all samples, as indicated by observed pores with diameters less than 2 nm (not shown in the figure). The main difference is observed in the peak intensity of the log differential intrusion, which indicates the number of pores in the sample. Mesopores with diameters less than 50 nm contribute most of the main sites for nitrogen gas adsorption in all samples. The plot of the log differential intrusion increases for samples from Z-30 to Z-60 and decreases for samples from Z-60 to Z-120. Increases and decreases in the log differential intrusion are attributed to corresponding changes in the abundance of mesopores with a wider distribution in the connected pore network. Thus, the Z-60 sample treated by microwave heating for 60 min has the largest abundance of interconnected mesopores. Their origins have been explained by the SEM images discussed previously.

Figure 4 shows the variation in oxygen purity for samples prepared by microwave treatment for different durations. Three adsorption performance phases can be distinguished in the PSA system: An initial increase, a plateau (stable phase), and a final rise in oxygen purity. In the initial phase, for all samples, the oxygen purity in ambient air before purification is 21%. After passing through the PSA system, the oxygen content begins to increase at t = 24 s and reaches its peak at 59.15% at t = 192 s for Z-30, 73.01% at t = 203 s for Z-60, 46.38% at t = 181 s for Z-90 and 38.64% at t = 168 s for Z-120. The oxygen purity increases at different rates, as shown in the inset of the figure, until it reaches its peak. The rate of increase in oxygen purity rises from Z-30 to Z-60 and then decreases from Z-60 to Z-120. **Figures 4** and **3(b)** show a notable correlation between oxygen purity and the intensity of the log differential intrusion. Therefore, the increase and decrease in the rate of oxygen purity are attributed to the corresponding increase and decrease in the abundance of interconnected mesopores formed in the samples. This result is consistent with experimentally measured values of oxygen generation in studies on nano zeolite adsorbent [32] and large microporous zeolite [20,33]. At the stable phase, increasing the microwave heating time from 30 min (Z-30) to 60 min (Z-60) has a significant effect, raising the highest peak value of oxygen purity from 59.15% to 73.01%. Further increasing the heating time from 60 min (Z-60) to 120 min (Z-120) results in a decrease in the peak value from 73.01% to 38.64%. The same trend is observed for the stable duration of the highest peak value, which increases from 216.6 s to 288.2 s as heating time increases from Z-30 to Z-60, then decreases from 288.2 s to 72.4 s. The increases and

decreases in peak values and stable duration are attributed to corresponding changes in the abundance of interconnected mesopores, as explained by the log differential intrusion in **Figure 3(b)**. In the final stage, the oxygen purity for all samples decreases as time increases, due to a reduction in adsorbed nitrogen in the pores as all accessible pores gradually become saturated. After saturation, a nitrogen/oxygen gas mixture rich in nitrogen is released.

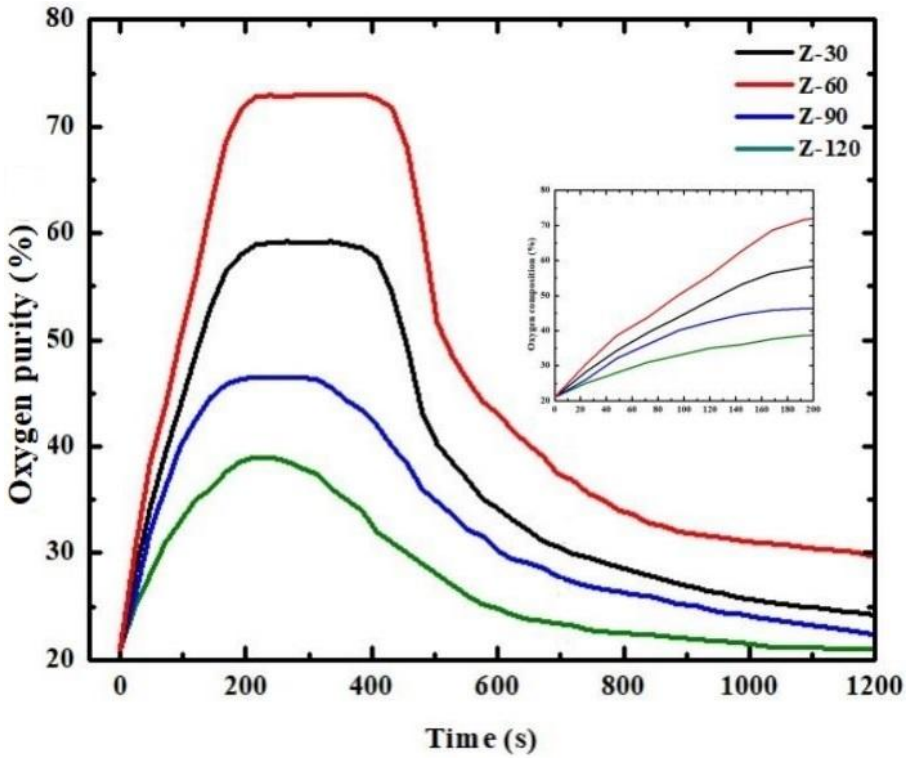

Figure 4 Variation of the oxygen purity for samples prepared by microwave treatment at different times.

Figure 5 shows FTIR spectra for TiO_2 cathode material of an Al-air battery after the first discharge, as a function of different oxygen purities. Peaks 1 and 2, at wavenumbers around 450 and 800 cm^{-1}, correspond to Ti–O and Ti–O–Ti stretching modes, respectively [34]. Peak 3 at 1,060 cm^{-1} is due to the bending vibration of the Al–O bond [35], which may indicate the presence of $Al(OH)_3$ formed from the reaction of Al^{3+} and OH^-. Peak 5 at 1,544 cm^{-1} corresponds to C–N stretching [35], resulting from nitrogen entering the carbon interlayer pores. The absorption at 1,632 cm^{-1} (peak 6) is attributed to water molecules. The broad absorption at 3,443.66 cm^{-1} corresponds to the O–H stretching mode of the hydroxyl group, indicating that moisture is bound in the sample [36]. **Figure 6** shows that the calculated integrated intensity of the Al–O bending mode at 1,060 cm^{-1} decreases as the oxygen purity increases from 21.00% to 73.01%. This decrease is related to an increase in the number of $Al(OH)_3$ layers in the sample, due to the reaction between the Al anode and a higher concentration of H_2O and lower partial pressure of oxygen within the pore at lower oxygen purity during the discharge process. These results are consistent with previous studies [37,38].

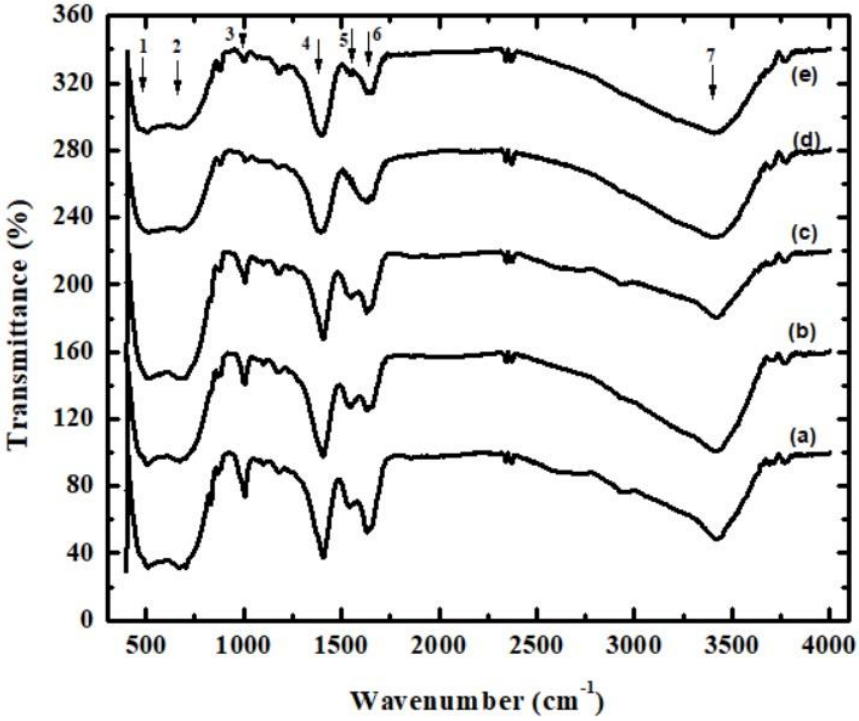

Figure 5 FTIR spectra for TiO_2 cathode material of Al-air battery after the first discharge as a function of oxygen purity of (a) 21.00%, (b) 38.64%, (c) 46.38%, (d) 59.15% and (e) 73.01%.

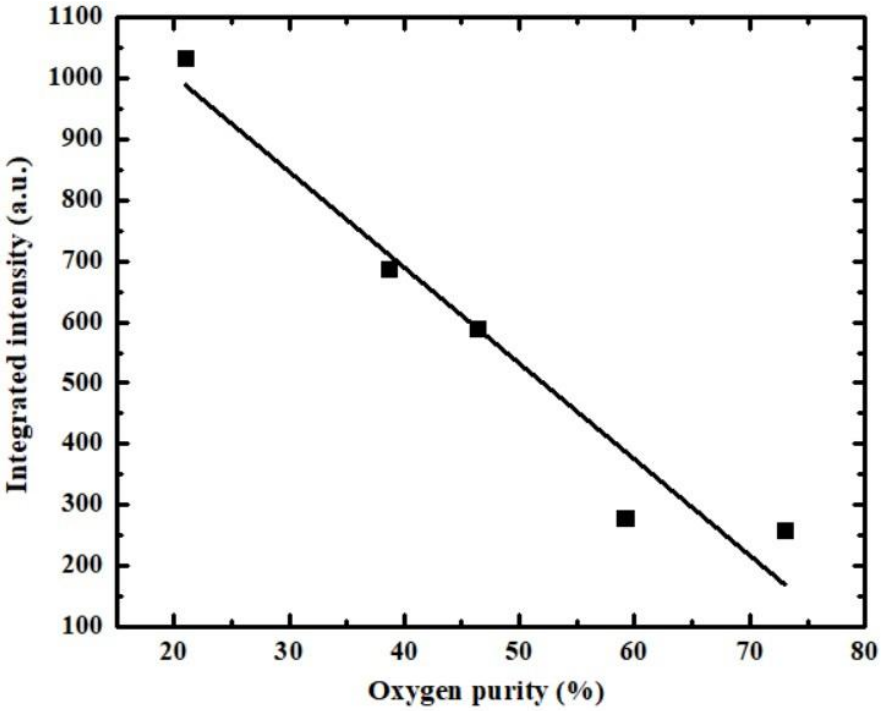

Figure 6 Calculated integrated intensity of Al-O bending mode for TiO_2 cathode material after the first discharge as a function of oxygen purity.

Figure 7 shows the variation in pore volume for TiO_2 cathode material after the first discharge as a function of oxygen purity. The general trend is that the volume of both micropores and mesopores increases with increasing oxygen purity. This increase in volume is attributed to a decrease in blockage of micropores and mesopores by $Al(OH)_3$ in both the interior and external surface pores of the sample. Pore blockage by $Al(OH)_3$

depends on the partial pressure of oxygen produced by chemical reactions in the pores, with higher purity oxygen gas resulting in a higher partial oxygen pressure [39]. All open pores on the external surface of the sample are blocked by $Al(OH)_3$ because the partial pressure of oxygen generated in the open space is too low to expel the $Al(OH)_3$ from the pore surface. The blockage of the interior pores occurs via a different mechanism, explained as follows. During consumption of oxygen at lower purity, a chemical reaction creates a lower partial pressure of oxygen within the interior pores, which expels only a small portion of $Al(OH)_3$, and alteration of the reaction pathway to prevent pore blockage in this case is incomplete. Thus, the consumption of oxygen results in most of the interior pores being blocked by $Al(OH)_3$. Consequently, the overall pore volume in the TiO_2 sample becomes smaller. When oxygen of higher purity is consumed, a reaction generates a higher partial pressure of oxygen within the interior pores, which expels the increased $Al(OH)_3$ and completely alters the reaction pathway to prevent pore blockage. In this case, the pressure interacts more actively with $Al(OH)_3$, causing the interior pores to enlarge. Consequently, the volume fraction increases in both micropores and mesopores. **Figure 7** also shows that the variation in volume is greater for mesopores than for micropores. This may be related to the larger number of interior and external surface pores in mesopores compared to micropores in TiO_2 samples.

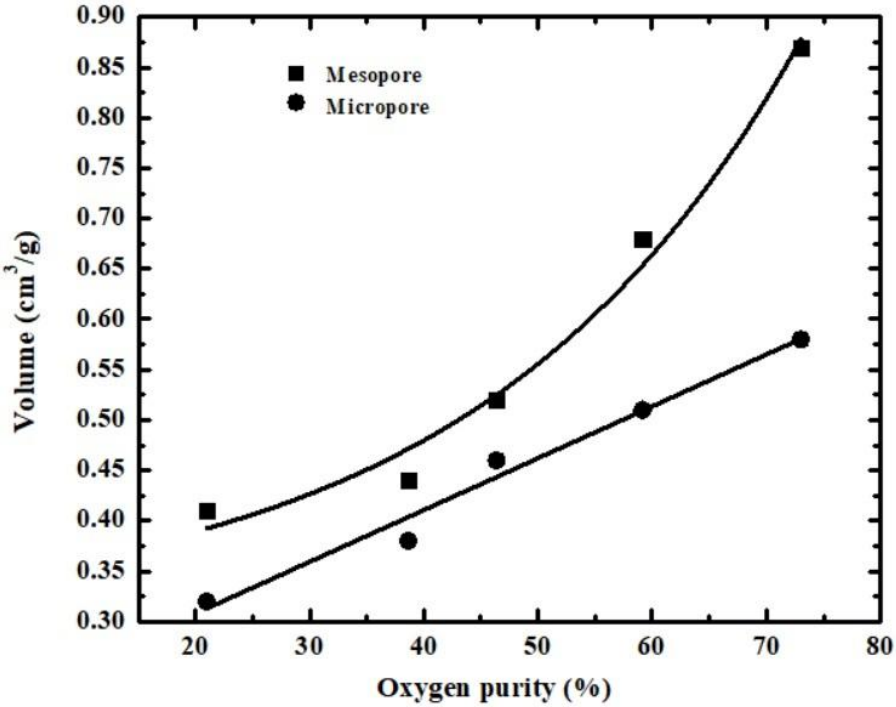

Figure 7 Variation in pore volume for TiO_2 cathode material after the first discharge as a function of oxygen purity.

Figure 8 shows the Nyquist plot of EIS spectra and the equivalent circuit model for the fitted EIS data (displayed in the inset) for Al-air batteries as a function of oxygen purity. All plots exhibit an approximately vertical straight line, a small semicircle in the intermediate-frequency region and a distorted large semicircle in the low-frequency region. The vertical straight line below the real impedance axis represents an inductive loop. The presence of these loops is related to the measurement cables and wires connecting the Al-air battery to the load during the EIS tests. The intersection of the small semicircles with the real axis in the Nyquist plot at high frequency indicates the electrolyte solution resistance [40]. This intersection decreases as oxygen purity increases. This phenomenon is due to the increased KOH electrolyte concentration at higher oxygen purities. The electrolyte concentration is determined by the amount of water solvent and higher oxygen purity leads to a greater concentration of dissolved oxygen in the electrolyte. Consequently, the

increased number of OH^- ions at higher electrolyte concentrations results in greater ionic conductivity. This effect shifts the entire EIS spectrum to lower impedance. This observation is consistent with previous findings, which showed that the solubility of oxygen in electrolytes increases with higher oxygen purity [41]. A small semicircle can be considered representative of the solid electrolyte interphase resistance (R_{SEI}). The R_{SEI} reflects the resistance of an interfacial layer formed by the decomposition of the electrolyte on the anode side. The diameter of the small semicircle decreases as the oxygen purity increases from 21% to 73.01%. The reason for the decrease in R_{SEI} with increasing oxygen purity is as follows. Impure oxygen entering the pores of the TiO_2 active material for electrochemical reactions is still contaminated by an inevitable mixture with H_2O. The reaction of Al metal with H_2O leads to corrosion and the formation of a passivation layer of $Al(OH)_3$ on the Al anode surface. When such layers form on the anode surface, they can hinder the electrolyte's access to the active material, thus reducing the battery's overall efficiency. With lower oxygen purity, the increase in RSEI can be attributed to a greater blocked surface area on the Al anode caused by the formation of the $Al(OH)_3$ layer. In this case, the reaction produces a larger volume fraction of the layer on the Al anode surface due to dissolved Al metal in solutions with higher H_2O content. Furthermore, with higher oxygen purity, the decrease in RSEI is attributed to a significant increase in the surface area of the Al anode exposed to the electrolyte. In this case, when Al is dissolved in a solution with lower water content, a smaller volume fraction of the layer forms. Several studies report results consistent with this study regarding the inhibition of electrolyte accessibility to the Al anode [42,43].

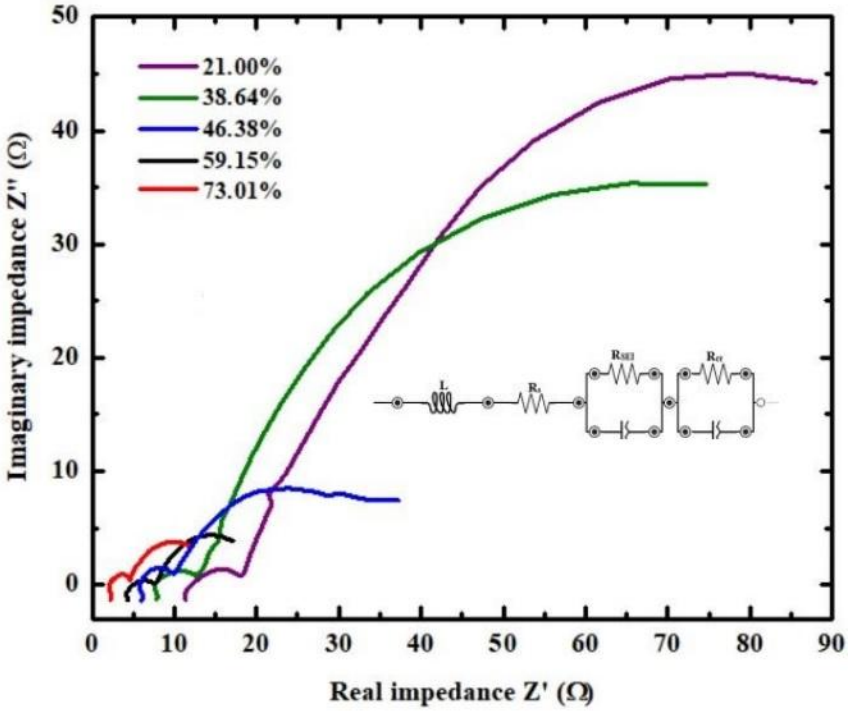

Figure 8 Nyquist plot of EIS spectra for Al-air batteries as a function of oxygen purity.

The large, irregular semicircle can be attributed to the impedance of the charge transfer reaction (R_{ct}). The semicircular curve decreases as oxygen purity increases from 21% to 73.01%. There are at least two origins of R_{ct}. The first arises from the ability of the TiO_2 cathode to facilitate the reduction of oxygen molecules (ORR) to water. Oxygen is adsorbed into the pores of the TiO_2 cathode and reduced via the ORR to hydroxide ions (OH^-). According to [44,45], the rate of oxygen diffusion during ORR is significantly influenced by oxygen purity. When oxygen purity increases from 21% to 73.01%, the rate of ORR increases, resulting in greater formation of OH^- ions. As OH^- ions become more abundant in the electrolyte, they can more easily

access the interface between oxygen, electrolyte and the TiO_2 cathode. Therefore, the R_{ct} value decreases. This interpretation is consistent with the results of related studies on metal–air batteries using lithium [46], magnesium [47] and sodium [48] as anodes. The second possible origin of R_{ct} is the blocking of pores on the internal and external surfaces of the TiO_2 cathode by the $Al(OH)_2$ layer. The R_{ct} value decreases because the amount of $Al(OH)_3$ attached to the pores is reduced as oxygen purity increases.

Figure 9 shows the variation of R_s, R_{SEI} and R_{ct} for the Al-air battery as a function of oxygen purity. The resistances were found to be proportional to the oxygen purity, except for R_{ct}. The trends of R_s and R_{SEI} correlate linearly with changes in oxygen purity, indicating that Rs and RSEI are determined by changes in oxygen purity. The decrease in the slope of the curves shows that the variation in resistance is greater for R_s than for R_{SEI}. This means that as oxygen purity increases, the rate of change in electrolyte concentration to a higher level is greater than the rate of blocking of the Al surface by $Al(OH)_3$. It is understandable that as oxygen purity increases, less $Al(OH)_3$ layer blocks the Al surface. This may be related to the fact that lower H_2O content reacts with the Al. Furthermore, a non-linear variation of R_{ct} with oxygen purity was observed. There is an inverse correlation between Rct and mesopore volume in **Figure 7**. Therefore, this decrease in R_{ct} is due to an increase in the volume fraction of interior mesopores in the TiO_2 cathode. This means that the decrease in R_{ct} occurs because there is an increase in pore blocking by $Al(OH)_3$. The non-linear behavior of R_{ct} is due to the presence of a non-uniform $Al(OH)_3$ layer distributed on both the external surface and interior pores of the TiO_2 cathode [49].

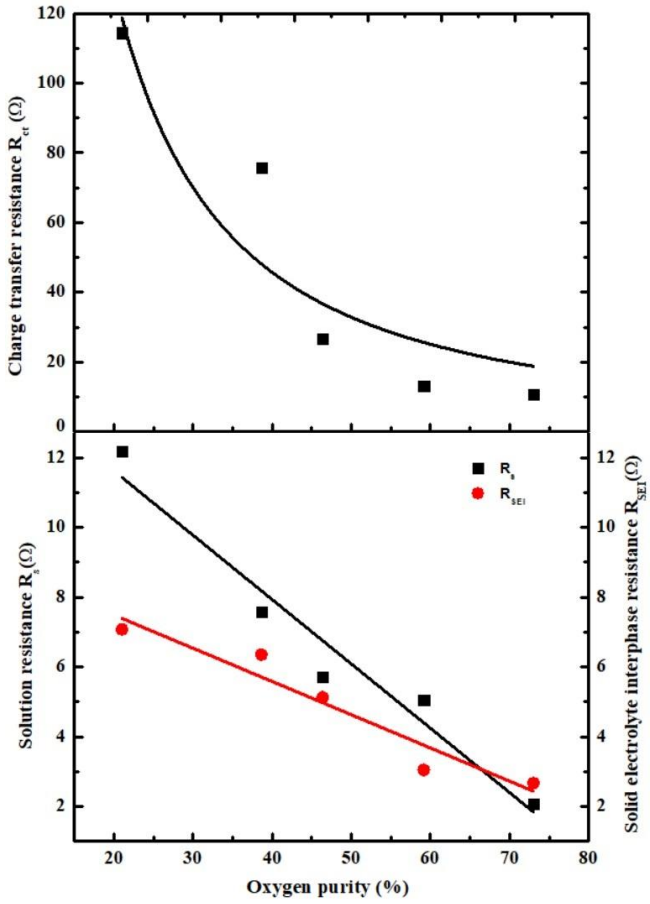

Figure 9 Variation of Rs, R_{SEI} and R_{ct} of Al-air batteries as a function of oxygen purity.

Figure 10 shows the discharge capacity performance of Al-air batteries as a function of oxygen purity. As oxygen purity increases, the battery's capacity also increases. At higher oxygen purities, batteries deliver greater capacities to store energy and provide higher power. At an oxygen purity of 73.01%,

Al-air battery cells typically produce a voltage of around 1.0 V, which matches the characteristic voltage value of an Al-air battery [50]. During the first few seconds of discharge, there is a sharp drop in voltage. The main cause of this decrease is the drying barrier of the electrolyte for the electron transfer reaction at the cathode. In this case, it is assumed that the electrolyte only penetrates the surface pores and has not reached the interior of the pore channels. As a result, there is uneven contact between the electrolyte and the active sites in the sample, leading to an initial voltage drop. Furthermore, when oxygen purity decreases, the cell voltage also decreases slightly. This decrease is due to an increase in R_s, measured as the internal resistance of the electrolyte to ionic flow. It was also found that the specific discharge capacity increased to 817.12 mAh/g as the oxygen purity increased to 73.01%. An increase in specific discharge capacity is related to a decrease in the measured R_{SEI} and R_{ct}. The EIS results indicate that at high oxygen purity, low R_{SEI} is due to the limited formation and growth of $Al(OH)_3$ on the Al anode surface. This layer reduces the loss of active anode material, thereby increasing the amount of OH^- ions generated in the pores, which aligns with interpretations from the literature [51]. Furthermore, the low R_{ct} of the TiO_2 cathode material results from reduced blockage of electrolyte entry into the micropores and mesopore channels by $Al(OH)_3$. In this case, more electrolyte ions can easily diffuse through the pores, allowing the reactions of oxygen and water to occur repeatedly and produce a higher amount of OH^- ions. Consequently, these processes enhance these stability of the Al-air battery and improve its discharge capacity. This interpretation is consistent with the observed behaviour of pore blockage by $Al(OH)_3$ for activated carbon [50], kaolin [52] and carbon fibre [53] cathodes in Al-air batteries.

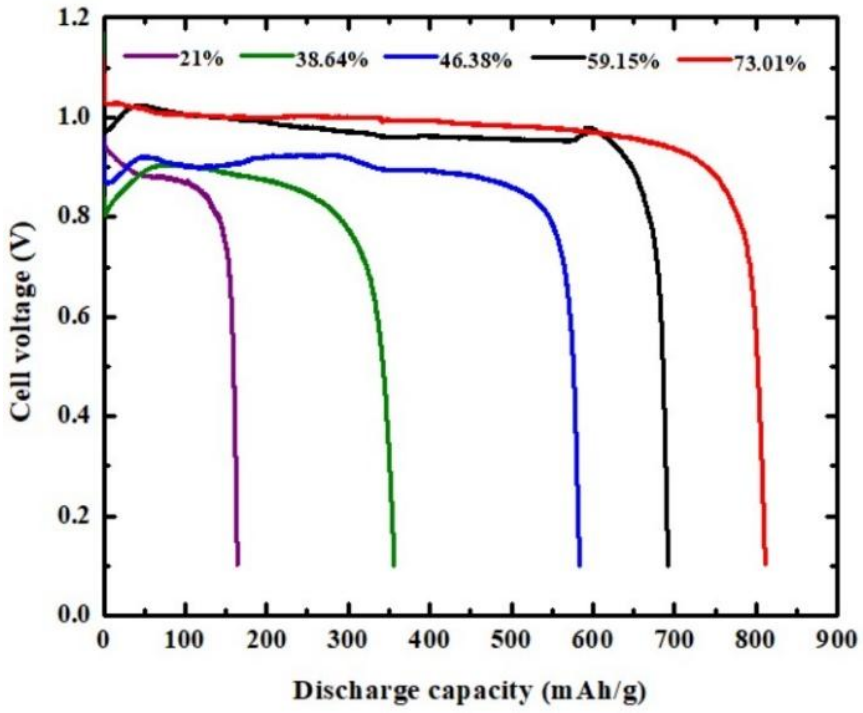

Figure 10 Discharge capacity performance of Al-air batteries as a function of oxygen purity.

Conclusions

The PSA system has successfully extracted high-purity oxygen from ambient air using a natural zeolite adsorbent. The prepared adsorbent has a mesoporous structure, with the relative proportion of pore volume depending on the heating time at 2.45 GHz in a microwave. A heating time of 60 min resulted in the highest proportion of mesoporous volume and produced the highest oxygen purity. Introducing high-purity oxygen as a cathode source affects the formation of

porous structures in the air cathode. The higher the purity of oxygen consumed by an Al-air battery, the smaller the amount of discharge products formed on the cathode surface, leading to the formation of more mesopores. Consequently, a higher discharge capacity is achieved. Our results indicate that high-purity oxygen is an effective approach to prevent the formation of pore-clogging discharge products on the cathode surface. This work demonstrates the technological feasibility of converting ordinary air into commercial oxygen or oxygen-enriched air for industrial processes related to battery storage and conversion technologies. The experimental results obtained in this study show that zeolite material has clear advantages and can be considered an appropriate and cost-effective adsorbent for industrial oxygen production using PSA technology.

Acknowledgments

This research was funded by the Ministry of Education, Culture, Research, and Technology, Republic of Indonesia, through the Project of Applied Research with Contract Number: 289/UN58.06/PM.00.00/2024. The authors also would like to thank Mr. Al-Gifari and Mr. Hahas Hasbullah for kindly helping to prepare the samples of the adsorbent material.

Declaration of Generative AI in Scientific Writing

The authors acknowledge the use of generative AI tools (e.g., QuillBot and ChatGPT by OpenAI) in the preparation of this manuscript, specifically for language editing and grammar correction. No content generation or data interpretation was performed by AI. The authors take full responsibility for the content and conclusions of this work.

CRediT Author Statement

H. Aripin: Conceptualization, Methodology, Supervision, Validation, Funding acquisition and Writing – original draft. **Rahmat Rizal:** Data curation, Formal analysis, Investigation, Validation and Visualization. **Irwan Muhammad Ridwana:** Formal analysis, Investigation, Validation and Visualization. **I Nyoman Sudiana:** Data curation, Formal analysis, Validation and Visualization. **Svilen Sabchevski:** Conceptualization, Resources, Software and Writing–review & editing.

References

[1] R El-Araby. Biofuel production: Exploring renewable energy solutions for a greener future. *Biotechnology for Biofuels and Bioproducts* 2024; **17**, 129.

[2] A Pitkaoja and J Ritvanen. Steam-oxygen blown circulating fluidised bed gasification for synthetic biofuel production: Pilot-scale reactor modelling, model-based reactor scale-up and analysis for power-biomass-to-liquid processes. *Biomass and Bioenergy* 2025; **193**, 107540.

[3] C Kodama, G Kuniyoshi, S Koya, M Salem, MM Othman, K Iwamoto, A Abubakar and R Brennan. Medical oxygen as a life-saving medicine: A rapid review of the oxygen landscape and innovative efforts in the World Health Organization eastern mediterranean region in response to COVID-19 and beyond. *Medical Research Archives* 2023; **11(7.2)**, 4162.

[4] Y Yuan, L Wang, Y Zhuang, Y Wu and X Bi. Energy and economic assessment of oxy-fuel combustion CO_2 capture in coal-fired power plants. *Energies* 2024; **17(18)**, 4626.

[5] IT Bello, LA Jolaoso, RA Ahmed and A Bello. Electrochemical energy conversion and storage systems: A perspective on the challenges and opportunities for sustainable energy in Africa. *Energy Reviews* 2024; **4(1)**, 100109.

[6] G Nazir, A Rehman, JH Lee, CH Kim, J Gautam, K Heo, S Hussain, M Ikram, AA Al-Obaid, SY Lee and SJ Park. A review of rechargeable zinc–air batteries: Recent progress and future perspectives. *Nano-Micro Letters* 2024; **16(1)**, 138.

[7] AG Olabi, ET Sayed, T Wilberforce, A Jamal, AH Alami, K Elsaid, SMA Rahman, SK Shah and MA Abdelkareem. Metal-air batteries: A review. *Energies* 2021; **14(21)**, 7373.

[8] M Salado and E Lizundia. Advances, challenges, and environmental impacts in metal–air battery electrolytes. *Material Today Energy* 2022; **28**, 101064.

[9] C Lv, Y Li, Y Zhu, Y Zhang, J Kuang, Q Zhao, Y Tang and H Wang. Quasi-solid-state aluminum–air batteries with ultra-high energy density and uniform aluminum stripping behavior. *Advanced Science* 2023; **10(29)**, e2304214.

[10] H Aripin, N Hiron, N Busaeri, FMS Nursuwars, L Faridah and S Sabchevski. Performance of Graphite/SiO_2 composites as cathode electronic active layer in Al-Air batteries. *In*: Proceedings of the IEEE International Conference on Sustainable Engineering and Creative Computing (ICSECC), Jakarta, Indonesia. 2020, p. 136-140.

[11] H Aripin, N Sutisna, N Busaeri and S Sabchevski. Enhancing power supply of Al-Air battery using an optimized conductive material of silica xerogel/graphite composite on an air cathode. *In*: Proceedings of the 10th International Conference on Chemical Science and Engineering, Springer, Singapore. 2023, p. 65-71.

[12] W Zhong, J Zhang, Z Li, Z Shen, S Zhang, X Wang and Y Lu. Issues and strategies of cathode materials for mild aqueous static zinc-ion batteries. *Green Chemical Engineering* 2023; **4(3)**, 264-284.

[13] J Xie and Y Wang. Recent development of CO_2 electrochemistry from Li-CO_2 batteries to Zn-CO_2 batteries. *Account of Chemical Research* 2019; **52(6)**, 1721-1729.

[14] R Singla and K Chowdhury. Enhanced oxygen recovery and energy efficiency in a reconfigured single column air separation unit producing pure and impure oxygen simultaneously. *Chemical Engineering and Processing - Process Intensification* 2021; **162**, 108354.

[15] A Imtiaz, MHD Othman, A Jilani, IU Khan, R Kamaludin, J Iqbal and AG Al-Sehem. Challenges, opportunities and future directions of membrane technology for natural gas purification: A critical review. *Membranes* 2022; **12(7)**, 646.

[16] R Šulc and M Kos. Experimental performance of pilot-oxygen-pressure swing adsorption unit. *Chemical Engineering Transactions* 2023; **100**, 223-228.

[17] C Chin, Z Kamin, MHV Bahrun and A Bono. The production of industrial-grade oxygen from air by pressure swing adsorption. *International Journal of Chemical Engineering* 2023; **2023**, 2308227.

[18] Y Sun, C Zhang, X Zhu, L Dong and X Sun. Mass and heat transfer of pressure swing adsorption oxygen production process with small adsorbent particles. *Processes* 2023; **11(8)**, 2485.

[19] M Al-Yousuf, RF Almilly and R Kamil. Methodological approach for optimizing production of oxygen by adsorption of Nitrogen from air using zeolite Li-LSX. *International Journal of Chemical Engineering* 2022; **2022**, 7254646.

[20] AF Al-Shawabkeh, N Al-Najdawi and AN Olimat. High purity oxygen production by pressure vacuum swing adsorption using natural zeolite. *Results in Engineering* 2023; **18**, 101119.

[21] N Caroko and Sukamta. Analysis of nitrogen adsorption capability at various activation temperatures of Klaten natural zeolite. *Jurnal Polimesin* 2024; **22(3)**, 305-309.

[22] JS Bobby, S Bharath, C Madhankumar, K Sudharsanam, U Ummathullah and PBE Prabhakar. Cost efficient oxygen concentrator with PSA technology. *Cardiometry* 2022; **25**, 182-185.

[23] H Aripin, N Busaeri, A Gufroni and S Sabchevski. Activated natural zeolite membrane for separating dissolved impurities in coconut sap. *Materials Science Forum* 2020; **1000**, 293-302.

[24] H Aripin, S Sutisna, E Priatn, IN Sudiana, E Surahman and S Sabchevski. Porous silica derived from sago waste and its application for the preparation of SiO_2/C composites as air cathodes for primary aluminum-air batteries. *International Journal of Electrochemical Science* 2022; **17(12)**, 221221.

[25] Z Adila, W Trisunaryanti and T Triyono. Modification of natural zeolite from Klaten, Indonesia using ammonium chloride by ion-exchange and its application as catalyst in ethanol dehydration to produce diethyl ether. *Indonesian Journal of Chemistry* 2024; **24(2)**, 505-518.

[26] V Novák, M Blazek, CM Schleputza, P Koci and M Stampanonia. Drying of water from porous structures investigated by time-resolved X-ray tomography. *Drying Technology* 2022; **40(16)**, 3675-3693.

[27] MR Mazlan, NH Jamadon, A Rajabi, AB Sulong, IF Mohamed, F Yusof and NA Jamal. Necking mechanism under various sintering process parameters e A review. *Journal of Materials Research and Technology* 2023; **23**, 2189-2201.

[28] TP Le, HVT Luong, HN Nguyen, TKT Pham, TLT Le, TBQ Tran and TNM Ngo. Insight into adsorption-desorption of methylene blue in water using zeolite NaY: Kinetic, isotherm and thermodynamic approaches. *Results in Surfaces and Interfaces* 2024; **16**, 100281.

[29] M Bossert, A Grosman, I Trimaille, F Souris, V Doebele, A Benoit-Gonin, L Cagnon, P Spathis, PE Wolf and E Rolley. Evaporation process in porous silicon: Cavitation vs pore-blocking. *Langmuir* 2021; **37(49)**, 14419-14428.

[30] C Ding, J He, H Wu and X Zhang. Nanometer pore structure characterization of taiyuan formation shale in the lin-xing area based on nitrogen adsorption experiments. *Minerals* 2021; **11(3)**, 298.

[31] DM Oliveira and AS Andrada. Synthesis of ordered mesoporous silica MCM-41 with controlled morphology for potential application in controlled drug delivery systems. *Ceramica* 2019; **65(374)**, 170-179.

[32] SM Faghih, M Salimi and H Mazaheri. Fabrication of Pebax/4A zeolite nanocomposite membrane to enhance CO_2 selectivity compared to pure O_2, N_2, and CH_4 gases. *International Journal of Engineering Transactions B: Applications* 2023; **36(2)**, 408-419.

[33] VK Yadav, N Choudhary, GK Inwati, A Rai, B Singh, B Solanki, B Paital and D Kumar. Recent trends in the nanozeolites-based oxygen concentrators and their application in respiratory disorders. *Frontiers in Medicine* 2023; **10**, 1147373.

[34] S Arunmetha, NR Dhineshbabu, A Kumar and R Jayavel. Preparation of sulfur doped TiO_2 nanoparticles from rutile sand and their performance testing in hybrid solar cells. *Journal of Materials Science: Materials in Electronics* 2021; **32**, 28382-28393.

[35] T Kolar, B Mušič, RC Korošec and V Kokol. Addition of $Al(OH)_3$ versus AlO(OH) nanoparticles on the optical, thermo-mechanical and heat/oxygen transmission properties of microfibrillated cellulose films. *Cellulose* 2021; **28**, 9441-9460.

[36] YV Fedoseeva, EV Lobiak, EV Shlyakhova, KA Kovalenko, VR Kuznetsova, AA Vorfolomeeva, MA Grebenkina, AD Nishchakova, AA Makarova, LG Bulusheva and AV Okotrub. Hydrothermal activation of porous nitrogen-doped carbon materials for electrochemical capacitors and sodium-ion batteries. *Nanomaterials* 2020; **10(11)**, 2163.

[37] M Rostami, AH Joshaghani, H Mazaheri and A Shokri. Photo-degradation of p-nitro toluene using modified bentonite based nano-TiO_2 photocatalyst in aqueous solution. *International Journal of Engineering Transactions A: Basics* 2021; **34(4)**, 756-762.

[38] P Katsoufis, V Mylona, C Politis, G Avgouropoulos and P Liano. Study of some basic operation conditions of an Al-air battery using technical grade commercial aluminum. *Journal of Power Sources* 2020; **450**, 227624.

[39] B Rani, JK Yadav, P Saini, AP Pandey and A Dixit. Aluminum-air batteries: Current advances and promises with future directions. *Royal Society of Chemistry Advances* 2024; **14(25)**, 17628-17663.

[40] M Wei, K Wang, L Zhong, THM Pham, Y Zuo, H Wang, P Zhang, Z Chen, S Zhao and P Pei. F^- competitive attack decomposing parasitic product $Al(OH)_3$ of hydrogel-based Al-air battery. *Energy Storage Materials* 2023; **60**, 102812.

[41] V Sivaprakash, L Natrayan, R Suryanarayanan, R Narayanan and P Paramasivam. Electrochemical anodic synthesis and analysis of TiO_2 nanotubes for biomedical applications. *Journal of Nanomaterials* 2021; **2021**, 9236530.

[42] F Bok, HC Moog and V Brendler. The solubility of oxygen in water and saline solutions. *Frontiers in Nuclear Engineering* 2023; **2**, 1158109.

[43] L Guo, Y Huang, AG Ritacca, K Wang, I Ritacco, Y Tan, Y Qiang, N Al-Zaqri, W Shi and X Zhen. Effect of indole-2-carboxylic acid on the self-corrosion and discharge activity of aluminum alloy anode in alkaline Al-Air battery. *Molecules* 2023; **28(10)**, 4193

[44] Y Zuo, Y Yu, H Shi, J Wang, C Zuo and X Dong. Inhibition of hydrogen evolution by a bifunctional membrane between anode and electrolyte of aluminum–air battery. *Membranes* 2022; **12(4)**, 407.

[45] HJ Kwon, HC Lee, J Ko, IS Jung, HC Lee, H Lee, M Kim, DJ Lee, H Kim, TY Kim and D Im. Effects of oxygen partial pressure on Li-air battery performance. *Journal of Power Sources* 2017; **364**, 280-287.

[46] J Li, F Yan, Z Su, T Zhang, X Zhang and H Sun. Highly efficient Li−air battery using linear porosity air electrodes. *Journal of The Electrochemical Society* 2020; **167(9)**, 090529.

[47] S Matsuda, M Ono, S Yamaguchi and K Uosaki. Criteria for evaluating lithium-air batteries in academia to correctly predict their practical performance in industry. *Materials Horizons* 2022; **9(3)**, 856-863.

[48] A Zhuk, G Belyaev, T Borodina, E Kiseleva, E Shkolnikov, V Tuganov, G Valiano and V Zakharov. Magnesium–air battery with increased power using commercial alloy anodes. *Energies* 2024; **17(2)**, 400.

[49] P Mao, H Arandiyan, SS Mofarah, P Koshy, C Pozo-Gonzalo, R Zheng, Z Wang, Y Wang, SK Bhargava, H Sun, Z Shao and Y Liu. A comprehensive review of cathode materials for Na-air batteries. *Energy Advances* 2023; **2(4)**, 465-502.

[50] H Wen, Z Liu, J Qiao, R Chen, G Qiao and J Yang. Ultrahigh voltage and energy density aluminum-air battery based on aqueous alkaline-acid hybrid electrolyte. *International Journal of Energy Research* 2020; **44**, 10652-10661.

[51] Y Zuo, Y Yu, H Shi, J Wang, C Zuo and X Dong. Inhibition of Hydrogen Evolution by a Bifunctional Membrane between Anode and Electrolyte of Aluminum–Air Battery. *Membranes* 2022; **12(4)**, 407.

[52] C Lv, Y Li, Y Zhu, Y Zhang, J Kuang, Q Zhao, Y Tang and H Wang. Quasi-Solid-State Aluminum–Air Batteries with Ultra-high energy density and uniform aluminum stripping behavior. *Advanced Science* 2023; **10(29)**, 2304214.

[53] WC Tan, LH Saw, MC Yew, D Sun, Z Cai, WT Chong and PY Kuo. Analysis of the polypropylene-based aluminium-air battery. *Frontiers in Energy Research* 2021; **9**, 599846.